


RESEARCH

Open Access



Gravimetric and morpho-structural analyses in the superhot geothermal system Los Humeros: an example from central Mexico

Natalia Cornejo-Triviño^{1,2*} , Domenico Liotta^{3,4}, Luigi Piccardi⁵, Andrea Brogi^{3,4}, Michal Kruszewski⁶, M.A Perez-Flores⁷, Jonathan Carrillo⁷, Philippe Calcagno⁸, Ingo Sass^{2,9} and Eva Schill^{1,2}

*Correspondence:
natalia.cornejo@kit.edu

¹ Institute for Nuclear Waste Disposal, Karlsruhe Institute of Technology (KIT), Karlsruhe, Germany

² Institute of Applied Geosciences, Technical University of Darmstadt, Darmstadt, Germany

³ Department of Earth and Geoenvironmental Sciences, University of Bari Aldo Moro, Bari, Italy

⁴ Institute of Geosciences and Earth Resources, National Research Council (IGG-CNR), Pisa, Italy

⁵ Institute of Geosciences and Earth Resources, National Research Council (IGG-CNR), Florence, Italy

⁶ Chair of Engineering Geology and Hydrogeology, RWTH Aachen University, Aachen, Germany

⁷ Earth Sciences Division, Center for Scientific Research and Higher Education (CICESE), Ensenada, Mexico

⁸ French Geological Survey (BRGM), Orléans, France

⁹ Geoenergy, German Research Centre for Geoscience (GFZ), Potsdam, Germany

Abstract

The influence of deep and regional geological structures is becoming increasingly important in superhot geothermal systems due to their proximity to the transition between brittleness and ductility. In the Los Humeros geothermal field in Mexico, where subsurface fluids reach temperatures of over 350 °C, the surface structures resulting from the collapse of calderas have so far only been interpreted at the local scale. The aim of this work is to place the recent tectonic and volcano-tectonic geomorphologic evolution and structures in the Los Humeros volcanic area in a regional context. NE- and NW-striking dominant structures resulting from a morpho-structural analysis on a regional scale are confirmed by negative and positive anomalies, respectively, after Butterworth filtering of gravity field data with different wavelengths over a local area of about 1000 km². By analyzing the slip and dilation trends of the observed directions, we show the relevance of the regional context for reservoir exploration. The magnitudes of the principal stresses we estimate indicate a trans-tensional fault regime, a combination of strike-slip and normal faulting. The structures derived from the gravity and morpho-structural analyses, which are parallel to the maximum horizontal stress, have the highest potential for tensile and shear failure. Therefore, the corresponding negative gravity anomalies could be related to fracture porosity. Consequently, we hypothesize that these structures near the transition between brittleness and ductility control fluid flow in the Los Humeros geothermal field.

Introduction

In geothermal systems with temperatures above 350 °C, referred to as superhot geothermal systems (SHGS), higher productivity can be achieved with fewer wells than conventional ones (Cladouhos et al. 2018). SHGS have been successfully drilled at depths near or within the brittle–ductile transition zone (BDT) in continental and oceanic crust (Kruszewski and Wittig 2018; Watanabe et al. 2019; Reinsch et al. 2017). To understand SHGS, the base of the permeable crust, which is controlled by fractures and in which geothermal fluids flow, albeit transiently, i.e., the depth of this regional rheological boundary, must be considered. This depends on various mechanical and

physical parameters, such as tectonic context, pressure, temperature, strain rate, lithology and fluid pressure (e.g., Kohlstedt et al. 1995).

The Reykjanes geothermal area in Iceland, for example, illustrates how the interaction of mechanical and physical parameters promotes brittle deformation: aseismic zones, such as those in the Reykjanes field, have been associated with low resistivity zones determined by inversion of magnetotelluric (MT) data (Sæmundsson and Einarsson 2014; Guðnason et al. 2015, 2016). Similar correlations have also been observed in other regions, e.g., in the Taupo Volcanic Zone in New Zealand and in the Villarrica low temperature field in southern Chile (Bertrand et al. 2012; Bryan et al. 1999; Pavez et al. 2020).

The Los Humeros geothermal field (LHGF), located in the eastern part of the Trans-Mexican Volcanic Belt (TMVB), does not have a clearly defined BDT. The northern part of the current production area has the highest temperatures of up to 380 °C at a depth of 2 km and is, therefore, a SHGS that has not yet been fully exploited. Inversion of MT data (Benediktsdóttir et al. 2019) shows anomalies with low resistivity trending N–S to NNW–SSE to a depth of 8 km. Seismic activity indicates brittle deformation to a depth of at least 3 km, as well as a heterogeneous stress state in different sectors of the field and at different depths (Lorenzo-Pulido 2008; Rodríguez et al. 2012; Lermo et al. 2016; Toledo et al. 2019, 2020; Jousset et al. 2019). Assuming a continental crust mechanically controlled by the rheology of quartz and a geothermal gradient of 100 °C/km, Calcagno et al. (2019) interpreted a BDT at about 4–4.5 km below the surface.

Given the relevance of deep structures for SHGS, in this study we complement the existing data from Los Humeros with gravity measurements, which can support integrated subsurface models (Calcagno et al. 2008; Guillen et al. 2008), and also provide valuable information on deep structures. Sequential Butterworth filters applied to the Bouguer anomalies reveal structures at different depth levels (Abdelfettah et al. 2014; Baillieux et al. 2014). Due to the spatial correlation of thermal and gravity anomalies (Baillieux et al. 2013), the latter has also been used to investigate fracture porosity in geothermal reservoirs (Baillieux et al. 2014; Altwegg et al. 2015). As such, gravity data physically characterize geologic lineaments. In the LHGF, the joint inversion shows a striking link between low density, low magnetization, and fault zones possibly related to hydrothermal alteration (Carrillo et al. 2022).

In addition, regionally distributed tectonic lineaments have proven to reflect the accumulation over time of deformation extending into the lower crust (Regenauer-Lieb and Petit 1997). Our morpho-structural approach involves a combination of tectonic geomorphology and structural geology, with the analysis of remote sensing imagery, digital terrain topography, multi-scale maps, local field mapping, and geological information to identify features of tectonic significance. This approach has been applied in active mountain chains (Piccardi et al. 1997, 1999; Boccaletti et al. 2002, 2001; Delle Donne et al. 2007; Nirta et al. 2021) and in volcanic areas (Boccaletti et al. 1998; Giaquinta et al. 1999; Pierotti et al. 2017; Piccardi et al. 2017) including the Los Humeros Volcanic Complex (LHVC) (Norini et al. 2019).

To investigate the relevance of the regional context to the reservoir exploration, the slip and dilation tendencies of the structures derived from gravity and morpho-structural results are analyzed based on a generic fault model (Morris et al. 1996; Ferrill

et al. 1999). Thus, we show which faults are favorably oriented to transmit geothermal fluids (Siler et al. 2016).

So far, the structures resulting from the caldera collapse in the LHGF have only been interpreted on a local scale (Norini et al. 2015; Carrasco-Núñez et al. 2017a). The present work aims to consider the recent tectonic and volcano-tectonic geomorphology of the Los Humeros volcanic area at a regional scale, characterize deep structures by gravity anomalies, and infer their geothermal relevance by analyzing their reactivation potential. In this way, we also contribute to defining of the local and regional BDT depth.

Geological setting

The Trans-Mexican Volcanic Belt

The TMVB is an almost 1000 km-long Neogene continental volcanic arc resulting from the subduction of the Cocos and Rivera plates beneath the North American plate. The evolution of the subduction system, as well as the nature of the crust beneath the belt, mainly control its large spatial and temporal variation, as well as its magma composition, encompassing several ancient fault systems that were partially reactivated at different times (Ferrari et al. 2012).

The main fault systems within the TMVB are described by Ferrari et al. (2012) (Fig. 1). The age of deformation suggests a coherent pattern of southward migration of tectonic activity. However, the fault system between Querétaro and Toluca in the center of the TMVB does not clearly show such as pattern of tectonic activity during the Pleistocene–Holocene. East of this fault system, the Neogene deformation is less intense.

The western part of the TMVB is characterized by the intersection of the E–W-trending Chapala, the N–S-trending Colima, and the NW–SE-trending Tépica-Zocoalco grabens, southwest of Lake Chapala. The central part is affected by W–E-trending Quaternary normal faults with known historical seismicity, whereas no major active faults have been documented in the eastern part of the TMVB (Suter 1991).

In central Mexico, results from Suter (1991) indicate a normal faulting stress regime with a minor left-lateral strike-slip component. The direction of the

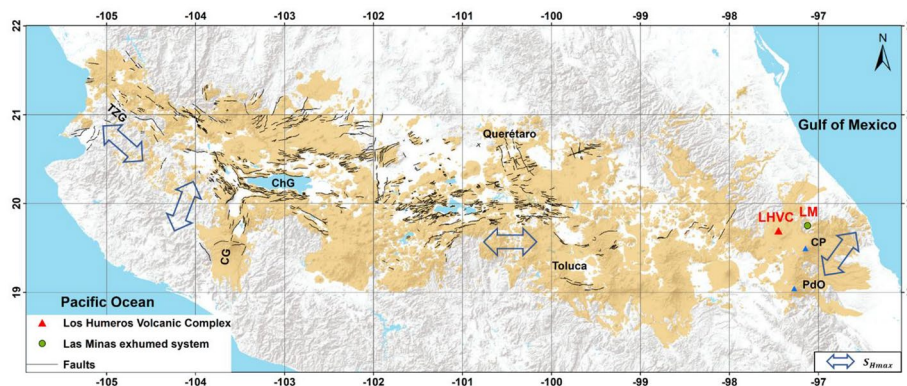


Fig. 1 Overview of the extension of the TMVB (beige color) and the location of the LHVC and Las Minas (LM). TZG: Tépica-Zocoalco graben. CG: Colima graben. ChG. Chapala graben. CP: Cofre de Perote. PdO: Pico de Orizaba. Main faults after Ferrari et al. (2012). Direction of the total maximum horizontal stress (S_{Hmax}) after Suter (1991) is indicated by double-headed arrows. DEM: Esri, USGS, NOAA

maximum total horizontal stress, S_{Hmax} , is shown in Fig. 1. Horizontal displacement vectors of a recent DGPS monitoring in Los Humeros show that the preferential extension orientation of the minimum total stress, S_3 , is NW–SE (García-Hernández et al. 2021).

The Los Humeros Volcanic Complex

The LHVC is a Pleistocene basaltic andesite–rhyolite explosive caldera volcano formed by two explosive eruptions encompassed between 460 and 70 ka (Ferriz and Mahood 1984; Carrasco-Nunez et al. 2012), followed by two minor post-caldera eruptive events, dated at 44.8 ± 1.7 and 2.8 ± 0.03 ka, respectively, the latter affecting the southern border of the caldera rim (Carrasco-Núñez et al. 2017b; Lucci et al. 2020). The LHVC holds an active geothermal system, the LHGF, located in the eastern sector of the TMVB (Fig. 1), northeast of the Pico de Orizaba-Cofre de Perote range (Carrasco-Núñez et al. 2017a). The location of the caldera is controlled by the intersection of pre-existing fault systems, NNW- and NE- oriented, respectively, determining an asymmetric caldera, with the deepest part settled in its south-western sector (Maestrelli et al. 2021, with references therein). Within the Los Humeros caldera, the volcano-tectonic structural system is controlled by the smaller Los Potrereros caldera, where faults deriving from the caldera collapse are oriented from NNW–SSE to E–W (Norini et al. 2015). A schematic geological map of the LHVC is presented in Fig. 2.

The caldera structure is well captured in the 3-D integrated geological model of Los Humeros proposed by Calcagno et al. (2022) (Fig. 3). This integrated scale of the model is based on the extent of the geophysical surveys performed during the GEMex project.

Holocene volcanism records the recurrent injection of compositionally distinct magma batches uprising from different crustal depths. This indicates the transition from the caldera stage magmatic system dominated by a single, large, and shallow magmatic body to a polybaric post-caldera stage plumbing system made up of a lower crust mafic reservoir feeding smaller magma batches that are vertically distributed (Carrasco-Núñez et al. 2022). The Los Humeros area is interpreted to be affected by the resurgence of the caldera floor (Norini et al. 2015; Toledo et al. 2020), induced by an inferred magmatic intrusion, representing the heat source of the geothermal system, exploited in the central and northern caldera areas (Arellano et al. 2003; Gutierrez-Negrin and Izquierdo-Montalvo 2010; Lelli et al. 2021).

Heterogeneous stress state in different sectors of the LHGF and at maximum depths of 3 km have been inferred (Lorenzo-Pulido 2008; Rodríguez et al. 2012; Lermo et al. 2016; Toledo et al. 2019; Jousset et al. 2019). However, the age of the caldera formation, the post-caldera plumbing system, and the hypothesized magmatic resurgence allow us to assume that the local variation of stress induced by the caldera collapse (Holohan et al. 2013; Corbi et al. 2015; Oliva et al. 2022) has stopped. In this study, we consider that the Los Humeros area is affected by regional tectonic stress as the primary driver, mainly controlling the present geothermal fluids pathways.

The exhumed Miocene geothermal system of Las Minas (shown in Fig. 1 with a green circle) is located 20 km to the northeast of Los Humeros. It is considered as an analog of the LHGF since it exposes rocks belonging to the Los Humeros pre-volcanic basement

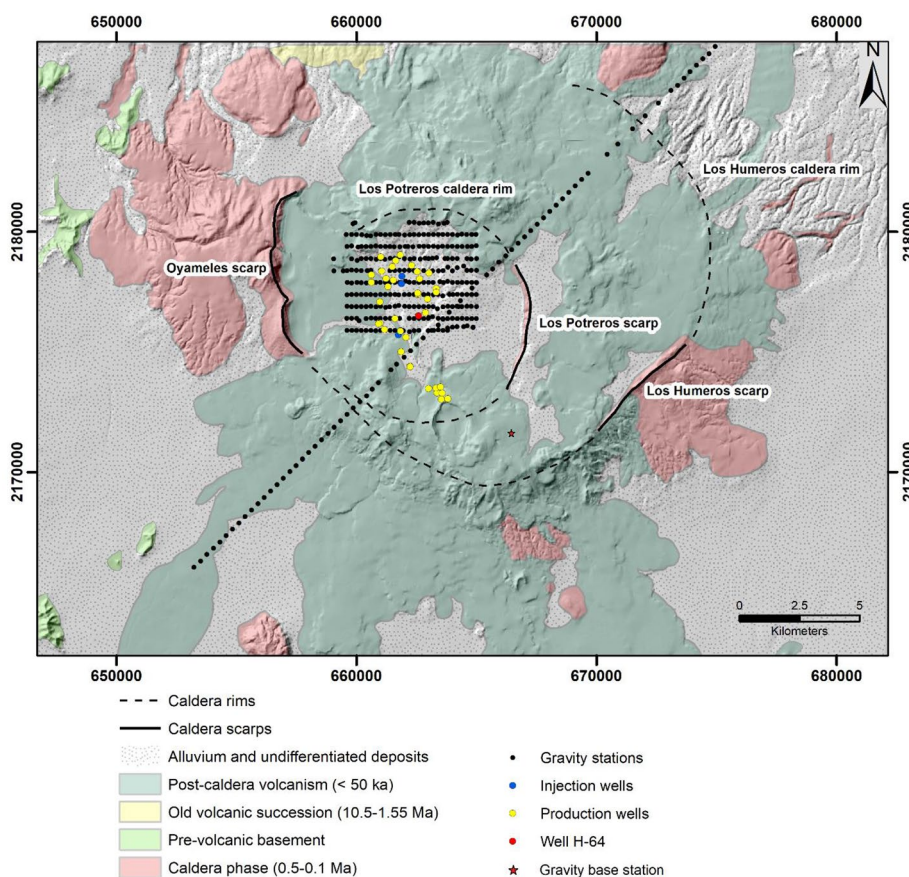


Fig. 2 Schematic geological map of the LHVC compared to the Digital Elevation Model (from Instituto Nacional de Estadística y Geografía, INEGI, Mexico) after Norini et al. (2015). The location of the LHVC within the TMVB is shown in Fig. 1

(Carrasco-Núñez et al. 2017a). According to Olvera-García et al. (2020a), two fault systems controlled dike emplacements and paleo-geothermal fluid flow: NE-striking normal faults and NNW-striking transfer faults.

Materials and methods

Morpho-structural analysis

With the aim of improving our understanding of the main trends in recent tectonic structures and volcanic-tectonic geomorphology, a morpho-structural analysis was carried out at the LHVC at local and regional scales. The analysis was based on remote sensing data such as topographic maps, rectified satellite images from Landsat, Google Earth, and Bing, digital elevation models, and geological maps at different scales.

This analysis was completed by fieldwork to fix pin-points for the remote sensing analysis. The field survey was performed mainly within the Pleistocene caldera area, the main target for geothermal exploration, as well as along other structures outside the caldera. Faults and fractures, as well as evidence of recent faulting affecting the volcanic deposits, were collected to verify some of the inferred structures and to learn about the local geomorphologic response of recent faulting in this volcanic area.

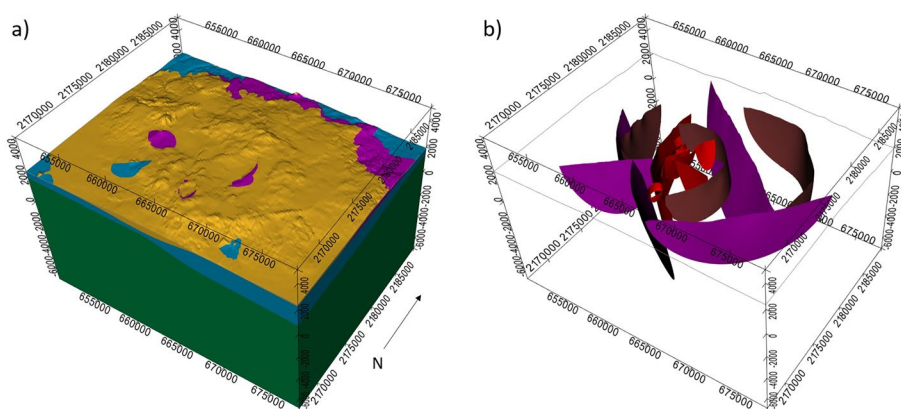


Fig. 3 **a** Integrated 3-D geological model of Los Humeros (Calcagno et al. 2022) with four geological groups: basement (green), pre-caldera (blue), rocks from the caldera (purple), post-caldera rocks (brown). **b** Visualization of the faults: regional faults (purple) and local faults (red)

Alignments of volcanic structures, especially within monogenic volcanic fields, were also mapped while paying attention to their morpho-structural characteristics. The criteria used to distinguish tectonic faults, although may be considered subjective, are based on tectonic-geomorphological considerations. For instance, a fault exhibiting a high scarp and longer and more accentuated lateral continuity is considered a major fault with respect to one that features subdued scarps and is laterally discontinuous (Piccardi et al. 1999).

As morpho-structures indicative of recent tectonics, we considered those geomorphological lineaments in laterally continuous scarps whose features suggest that they could be related to tectonics affecting younger geological or geomorphological elements, such as lava deposits, volcanic features (such as crater rims, alignment of monogenic cones or volcanic centers) or dated paleosurfaces. The simultaneous presence of several pieces of geomorphologic, volcanic-tectonic, or field mapping evidence confirm their tectonic origin. Examples of the methodology described can be found in the Additional file 1.

Gravity data

In the following, we describe the procedures of data acquisition and processing, and the forward modeling of the gravity response of the 3-D geological model (Fig. 3). Section “[Filtering analysis](#)” describes the concept of Butterworth filtering. It should be noted that the comparison with the results of the morpho-structural analysis is based on the Butterworth-filtered data.

Survey and processing

Gravity data in the LHGF was acquired during two field surveys (November–December 2017 and April 2018) in an area of 24 km × 23.5 km during the GEMEX project (www.gemex-h2020.eu; Fig. 2) using a CG-5 Autograv with an instrumental accuracy of 0.001 mGal. The positions were measured by differential GPS (DGPS) using two Trimble 5700 receivers and two Trimble antennas with an instrumental

vertical accuracy of 5 mm. From the 344 gravity measurements, 263 were acquired along ten E–W profiles of 5.5 km length with typical inter-station and inter-profile distances of 200 and 500 m, respectively. The survey was completed by a NE–SW oriented, 31-km-long profile, including 81 gravity measurements with an inter-station distance of about 375 m. Three measurements were rejected due to unreliable DGPS records.

Standard deviations of the raw data measurements range between 0.008 and 0.119 mGal and between 0.0012 and 0.3893 m for the gravity (Fig. 4a) and the vertical component of the DGPS data (Fig. 4b), respectively. The application of thresholds of 0.05 mGal and 0.2 m results in a final number of 318 stations for further processing, i.e., 92.4% of the acquired data.

Instrumental drift, earth tide, latitude, and elevation corrections were carried out using GravProcess Matlab codes (Cattin et al. 2015). To estimate the instrumental drift, repeated gravity measurements were carried out at the beginning and end of each day of measurements at a base station (red star in Fig. 2). The instrumental drift correction was estimated by a least-squares fit of the weighted time series at this station with a first-order polynomial function. The earth tide correction was calculated for each gravity measurement according to Agnew (2007, 2012). Free-air and simple Bouguer corrections were made using the DGPS-processed data.

A complete Bouguer anomaly (Kane 1962; Nagy 1966) was obtained using a Bouguer density of 2670 kg m⁻³. The terrain correction was carried out using the Oasis Montaj™ software (Geosoft) up to a maximum distance of 166.7 km from each gravity station (LaFehr 1991). Since the gravitational effect of a prism decreases with the square of the distance, digital elevation models (DEM) were used with the following resolutions, which decreases with increasing distance from the gravity stations:

- a. from each station to 10 m: 1 m (courtesy of Centro Mexicano de Innovación en Energía Geotérmica);
- b. from 10 m to 1 km: 15 m (courtesy of Instituto Nacional de Estadística y Geografía);
- c. from 1 to 10 km, (b) resampled to 50 m;
- d. from 10 to 100 km, (b) resampled to 500 m; and

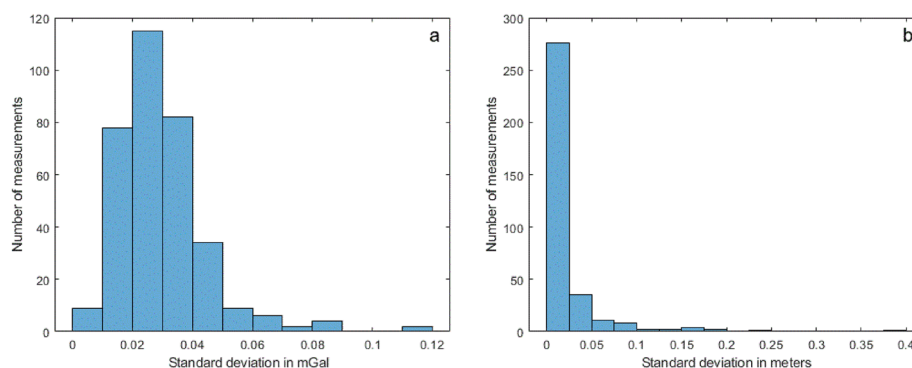


Fig. 4 Standard deviation of the **a** gravity and **b** vertical component of the differential GPS measurements. Standard deviation windows of 0.05 mGal and 0.2 m, respectively

e. from 100 to 167 km, (b) resampled to 5 km.

Note that for the 14 north-easternmost stations the 1 m DEM was not available and thus the 15 m resolution DEM was the highest resolution used in the terrain correction.

Given the standard deviation threshold of the GPS measurements, the uncertainty introduced by the terrain correction is estimated to be below 0.06 mGal. The uncertainty in elevation introduced by the DEM is approximately 0.6 mGal, summing up with the standard deviation threshold of the gravity measurements (0.05 mGal) to a mean uncertainty of about 0.7 mGal.

The complete Bouguer anomaly in the LHGF (Fig. 5) was complemented with a regional complete Bouguer anomaly with a reference density of 2670 kg m^{-3} including 13,737 measurements (courtesy of Comisión Nacional de Hidrocarburos). The regional trend represents the increase in crustal thickness from the Gulf of Mexico towards the center of the continent (Urrutia-Fucugauchi and Flores-Ruiz 1996). From this comprehensive data set, the residual anomaly was determined by subtracting the regional trend (Fig. 5b) in the area of the geological model. The latter was determined using a Gaussian filter with a cutoff wavelength of 20.5 km. The respective radially averaged power spectrum of the complete Bouguer anomaly is included in Additional file 1: Fig. S6.

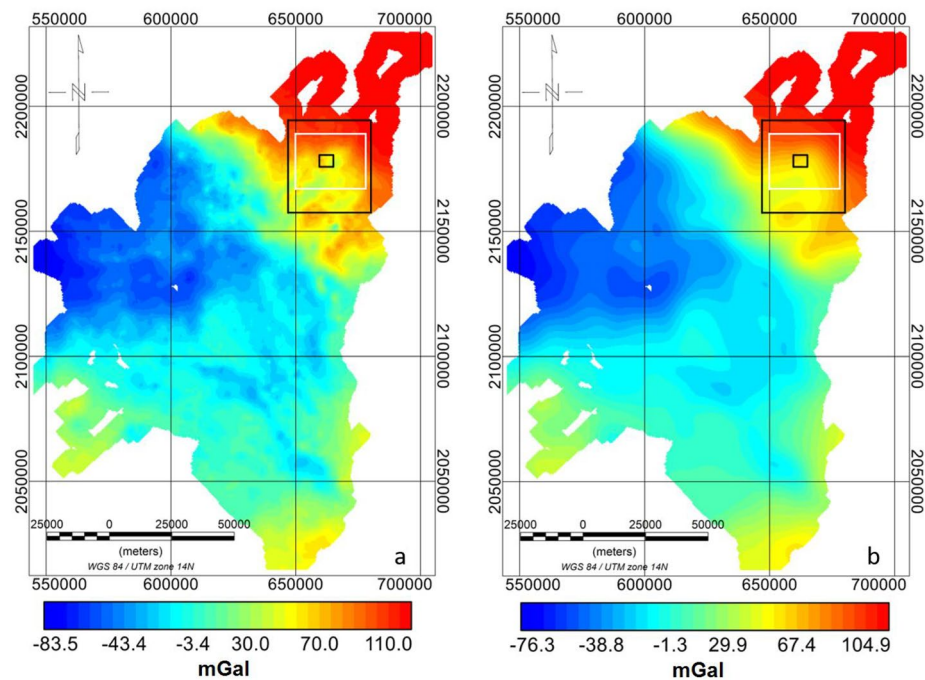


Fig. 5 **a** Interpolated regional complete Bouguer anomaly using a density of 2670 kg m^{-3} provided by the Comisión Nacional de Hidrocarburos (<http://www.gob.mx/cnh>). **b** Regional trend of the complete Bouguer anomaly using a Gaussian filter. Inner/outer black rectangles delineate the areas of the processed gravity data in the LHGF and Butterworth filtering analysis, respectively. The white rectangle shows the area of the 3-D geological model

Table 1 Average bulk density values, ρ_{bulk} , and standard deviation of analogue samples of the geological groups of LHGF and Las Minas (Weydt et al. 2021) used in the forward modeling

Geological group	ρ_{bulk} [kg m ⁻³]
G1 Post-caldera	1663 ± 113
G2 Caldera	1490 ± 184
G3 Pre-caldera	2174 ± 174
G4 Basement	2635 ± 135

Table 2 Wavelength ranges of the high- and band-pass filters applied to the complete Bouguer anomaly

Butterworth filters	Wavelength in km
High-pass	6, 10, 20
Band-pass	6–10, 6–30, 10–30

Forward modeling

Gravity forward modeling was performed to investigate the validity of the integrated 3-D geological model (Fig. 3) using GeoModeller software (Intrepid Inc.; Calcagno et al. 2018; Guillen et al. 2008), which calculates the gravity response based on the equations of Plouff (1976), Okabe (1979), and Holstein (2003). The average bulk density values were taken from Weydt et al. (2021) (Table 1).

Due to the uniform geology below 0 m.a.s.l., where only basement occurs, we limit the forward modeling to this depth. The geological model was discretized into 3-D voxels with a minimum cell size of 210 m in the X and Y directions, resulting in a horizontal cell distribution of $n_x = 133$ and $n_y = 104$. In the vertical dimension, a variable cell size between 131 and 151 m with a geometric factor of 1.1 was used, resulting in a number of vertical cells of $n_z = 32$. Finally, each voxel of the geological model is associated with a stratigraphic unit and its respective density value.

Filtering analysis

To place the filter analyses in a regional context, a subset of 1083 regional gravity field stations was added to the local survey (see outer black rectangle in Fig. 5). The spatial data of the full Bouguer anomaly were transformed to the wavenumber domain by a fast Fourier transform and Butterworth filters (Butterworth 1930) were defined and applied using Oasis Montaj™ software (Geosoft). In this context, the spatial data of the study area are extended to ensure continuity and periodicity. It is then interpolated to make it periodic along both coordinates. For reference and analysis purposes, the radial average spectrum is calculated, and high-pass and band-pass filters are defined and applied. The full wavelength ranges of the high-pass and band-pass Butterworth filters used are listed in Table 2. As a first approximation, it is assumed that a longer wavelength represents deeper structures.

Slip and dilation tendency analysis

Generic slip and dilation tendencies (Morris et al. 1996) were calculated and compared to the observed orientations of the residual gravity anomalies and the structures identified during the morpho-tectonic analysis.

The regional stress in Los Humeros and surrounding areas is defined by a NE-trending maximum horizontal stress with an azimuth, $\theta_{S_{Hmax}}$, of $42^\circ E \pm 8^\circ$ (Heidbach et al. 2016) and a dominant NNW-trending crustal extension direction (García-Palomo et al. 2018). This stress field interacts with the crustal uplift indicated by the high heat flow in the TMVB (Prol-Ledesma et al. 2018; Prol-Ledesma and Morán-Zenteno 2019; Espinoza-Ojeda et al. 2023). Seismic tomography (Toledo et al. 2020) suggests a caldera resurgence in the Los Humeros area, which implies that uplift is dominant with respect to crustal extension today.

The stresses are therefore calculated in two ways: (i) inside the caldera, where the geothermal fluid pressure is active (pore fluid factor $\lambda = 0.9$; cfr. Liotta and Ranalli 1999), and (ii) outside the caldera, where the fluid pressure is assumed to be hydrostatic ($\lambda = 0.4$).

In this study, we estimate the horizontal effective principal stresses based on linear elasticity assumptions (Thiercelin and Plumb 1994):

$$\sigma_{Hmax} = \frac{\nu}{1 - \nu} \sigma_v + \frac{E}{1 - \nu^2} \varepsilon_{Hmax} + \nu \frac{E}{1 - \nu^2} \varepsilon_{hmin},$$

$$\sigma_{hmin} = \frac{\nu}{1 - \nu} \sigma_v + \nu \frac{E}{1 - \nu^2} \varepsilon_{Hmax} + \frac{E}{1 - \nu^2} \varepsilon_{hmin},$$

where ν is the rock's static Poisson's ratio and E is the rock's static Young's modulus, both taken from Weydt et al. (2021). Total vertical principal stress, S_v , and pore pressure, P_p , gradients to calculate the effective vertical stress (σ_v) were obtained from Kruszewski et al. (2022).

The minimum, ε_{hmin} , and maximum tectonic strains, ε_{Hmax} , were determined on the basis of a 1-D geomechanical model using a strain-corrected method (Thiercelin and Plumb 1994; Blanton and Olson 1999) and neglecting thermal effects. The geomechanical model developed was based on the results of the H 64 well (red circle in Fig. 2), including the lithologic column and elastic rock properties, and was calibrated using the stress values obtained from a leakage test in the same well (Kruszewski et al. 2022). The resulting tectonic strain amounted to ε_{hmin} of $-4.0 \pm 9.0 \cdot 10^{-5}$ and ε_{Hmax} of $127 \pm 34.1 \cdot 10^{-5}$.

We estimate the effective principal stresses to the top of the BDT as this is the base of crustal permeability controlled by fractures and where the flow of geothermal fluids is channeled. However, this is an approximation for a gradual transition that likely extends over several kilometers. By equating the critical stress for frictional failure and the creep stress in the ductile state, the BDT depth can be estimated as follows (Ranalli 1995, 1997; Liotta and Ranalli 1999):

$$\alpha \rho g z (1 - \lambda) = (\epsilon / A)^{1/n} \exp[E/nRT(z)],$$

Table 3 Frictional and creep parameters used in the BDT calculation

Frictional parameters			Creep parameters		
α	ρ [kg/m ³]	λ	A [MPa ^{-2.3} s ⁻¹]	n	E [Jmol ⁻¹]
0.68	2670	0.4–0.9	3.2×10^{-4}	2.3	154000

Assuming a continental crust that is mechanically governed by quartz's rheological behavior, parameters for wet quartz-controlled rheology were chosen (Ranalli 1995, 1997)

where α is a parameter that depends on the tectonic regime and the frictional properties of faults (here, $\alpha = 0.68$, assuming a coefficient of friction of 0.6 and normal faulting), ρ is the density of overlying rocks, g the acceleration of gravity, z the depth, λ the pore fluid factor (a ratio of pore fluid pressure to the lithostatic stress), ϵ the ductile strain rate, R the gas constant, T the absolute temperature, and A , n , and E the creep parameters of the rock (see Table 3).

Frictional parameters were chosen assuming a normal faulting regime (Sibson 1974) and a coefficient of friction of 0.6 (Byerlee 1978). Creep parameters were chosen assuming a quartz-dominated crust (Calcagno et al. 2019). Different pore fluid factors were considered in the analysis, from 0.4 (low pore fluid pressure) to 0.9 (high pore fluid pressure). In the ductile regime, we considered tectonic strain rates between 10^{-16} s^{-1} and 10^{-14} s^{-1} as references.

Regarding the temperature gradient considerations, more than 3800 new geothermal gradients were compiled by Espinoza-Ojeda et al. (2023) from deep boreholes. In the Los Humeros area, an average geothermal gradient of about $120 \text{ }^\circ\text{C km}^{-1}$ was estimated (data can be downloaded from: https://github.com/omespinozaojeda/Mexico_HF_database.git), and in the whole TMVB province, a geothermal gradient above $80 \text{ }^\circ\text{C km}^{-1}$ is expected in most areas (Prol-Ledesma and Morán-Zenteno 2019). The BDT depth was then calculated taking into account two geothermal gradients, one representing the geothermal area and the other the regional environment.

As slip and dilation tendencies strongly depend on the azimuth of the fault plane, the analysis was performed for a set of generic faults (Meixner et al. 2016) with fault plane azimuths from 0 to 180° and mean dip angles of 70° (Additional file 1: Table S1) under the estimated stress field.

Results

In the following, the lineaments obtained from the morpho-structural analysis is presented to show the predominant tectonic structures and their orientation. In Section "From the complete Bouguer to the residual anomaly", we present the residual anomaly after subtraction of the regional trend. We compare this residual anomaly with the gravity forward model of the integrated 3-D geologic model (Section "Forward modeling results compared to the residual anomalies") to demonstrate significant agreement within the caldera. Finally, in Section "High- and band-pass Butterworth filter results", we present sequential Butterworth filtering to decipher structures outside the caldera from the gravity field data. The results from the gravity field data point in sub-parallel directions to the morpho-tectonic results, and are thus used for the petrophysical characterization of the same.

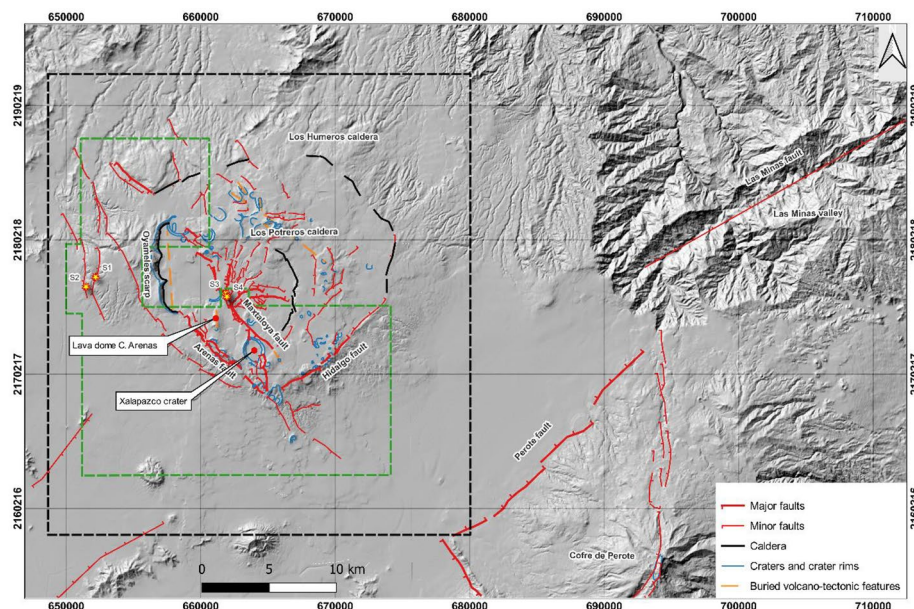


Fig. 6 Regional structures of the LHVC inferred from a morpho-structural analysis of the eastern sector of the TMBV. The black dashed rectangle delineates the area of the Butterworth filtering analyses (Fig. 5). The green dashed rectangle delineates the area of the morpho-structural analysis shown in detail in Additional file 1: Figs. 1–5

Morpho-structural analysis results

The regional structures of the LHVC, which were derived from a morpho-structural analysis of the eastern sector of the TMBV, are shown in Fig. 6. A detailed description of the recognized morpho-structures can be found in Additional file 1: Figs. S1–S5. The following structural trends were identified:

1. NE–SW oriented structures visible in the Las Minas valley and Los Humeros (e.g., the Perote fault). In the volcanic complex, NE–SW oriented major faults such as the Hidalgo Fault controls the southeastern side of the Los Humeros caldera (Fig. 6). Other similarly oriented structures are present inside and outside the volcano.
2. NW–SE oriented structures, visible in the southwest of the Cofre de Perote volcano, delimit the extent of the Perote fault. In the volcanic complex, the NW–SE oriented structures are the Mextaloya Fault, one of the main volcanic-tectonic structures controlling the LHGF and the Arenas Fault. A relevant buried volcanic-tectonic structure northeast of the Los Potreros caldera also has this orientation.
3. The most significant of the N–S oriented smaller structures are located in the western part of the Los Humeros caldera in the area of Oyameles and in the eastern part of the Los Potreros caldera. In addition, N–S oriented structures appear to control the emplacement of the N–S elongated lava dome of C. Arenas and the Xalapazco crater south of Los Humeros.
4. East–west oriented structures: These are manifested at the surface by minor faulting. This trend appears to have some control over the northern margin of the Los Humeros volcanic edifice.

Compared to the NW–SE, the NE–SW oriented structures may be older, as the former appear to control the regional tectonic evolution of the area. The Perote and Las Minas faults, as well as the subsided basin in the southwest of the Las Minas valley are examples. The N–S oriented structures generally have a limited extent and abut the major tectonic faults. They are therefore younger and determined by the latter. This applies, for example, to the lava dome of C. Arenas, the Xalapazco crater and the western structures of the Los Humeros caldera, which abut the NW–SE oriented faults. E–W oriented minor faults could be controlled by subsidence; however, subsidence due to soil compaction is not the subject of this paper as it requires further investigation for proper evaluation. Faulting in the central area of the LHVC is more likely to reflect local subsidence due to magmatic fluctuations or other effects related to the geothermal system. The fault kinematic indicators show that the Maxtaloya/Humeros fault and other major faults are mostly normal with an average dip of 70°. An overview of the kinematic indicators observed on the main fault structures in the Los Potreros caldera is provided in Additional file 1: Fig. S7 and Table S1.

Gravity results

From the complete Bouguer to the residual anomaly

The regional trend of increasing gravity values from SW to NE in the complete Bouguer anomaly (Fig. 7a) is eliminated in the residual anomaly of the area (Fig. 7b). In the latter, lowest residual gravity values are observed in the North–Eastern part of the LHGF and the Los Humeros caldera (Fig. 7b). Medium residual anomalies are observed to the SW of the caldera, trending NW–SE and SW–NE.

Forward modeling results compared to the residual anomalies

The forward model of gravity (Fig. 8) roughly reproduces the low anomaly in the central part of the Los Humeros caldera, but there is no further correlation between the calculated and observed gravity. This is especially true for the southwest of the forward modeled area. In contrast to a relatively high anomaly in the forward modeling, the residual anomaly map (Fig. 7b) shows a low anomaly that crosses the caldera and extends in the

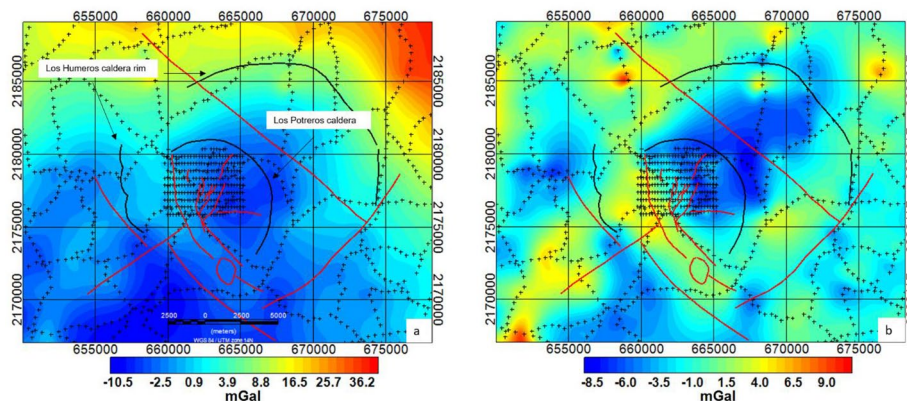


Fig. 7 **a** Complete Bouguer anomaly of the modeled area. **b** Residual anomalies of the LHGF and surroundings. Black crosses indicate gravity stations. Red and black lines represent major faults and the boundaries of the caldera, respectively (Calcagno et al. 2022)

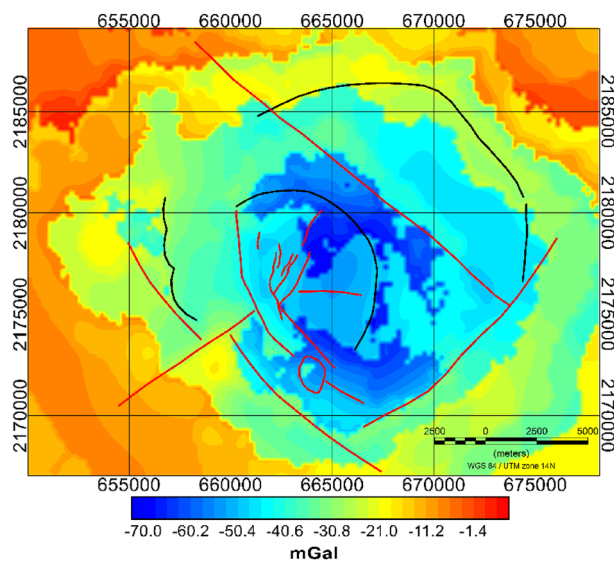


Fig. 8 Gravity response obtained from forward modeling of the 3-D geological model of Los Humeros (limited to 0 m.a.s.l.). Red and black lines represent major faults and the boundaries of the caldera, respectively (Calcagno et al. 2022)

NE–SW direction. To the southwest of the central region of the caldera, the residual anomaly shows intermediate anomaly values in the NW–SE direction, in contrast to the low anomaly observed in forward modeling (Fig. 8). Less pronounced alignments are observed in the NE–SW direction (Fig. 8).

The observed discrepancies are further investigated by sequential Butterworth filtering to understand the influence of potentially deep structures on the gravity data.

High- and band-pass Butterworth filter results

Considering the accuracy of our gravity measurements of 0.7 mGal, the 3-km high-pass filter was not included in the analysis. High-pass and band-pass filters with increasing wavelengths from 6 to 20 km and 6 to 30 km, respectively, applied to the complete Bouguer anomaly are shown in Fig. 9a–c and d, e. To investigate the potentially deep structures, we show a wavelength band of 10–30 km (Fig. 9f).

Randomly distributed low- and high-gravity anomalies are observed in the 6-km high-pass filter (Fig. 9a). Although the dynamics of the 6-km filters extend over several mGal and the size of the anomalies is confirmed in the range of the data collected in this study (inner black rectangle in Fig. 5), it is not interpreted further. At a corner wavelength of 10 km, the previously randomly distributed anomalies begin to align (Fig. 9b). A group of negative anomalies surrounded by positive anomalies forms in the center of the Los Humeros caldera. In the southwest and northeast of the study area, the negative anomalies are oriented in a NE–SW direction and the positive anomalies are preferentially oriented in a NW–SE direction at a higher corner wavelength of 20 km (Fig. 9c). The anomalies observed at this filter level seem to correspond to the anomalies observed after subtracting the regional trend determined with the Gaussian filter (Fig. 7b). This indicates that the regional structures are represented by wavelengths

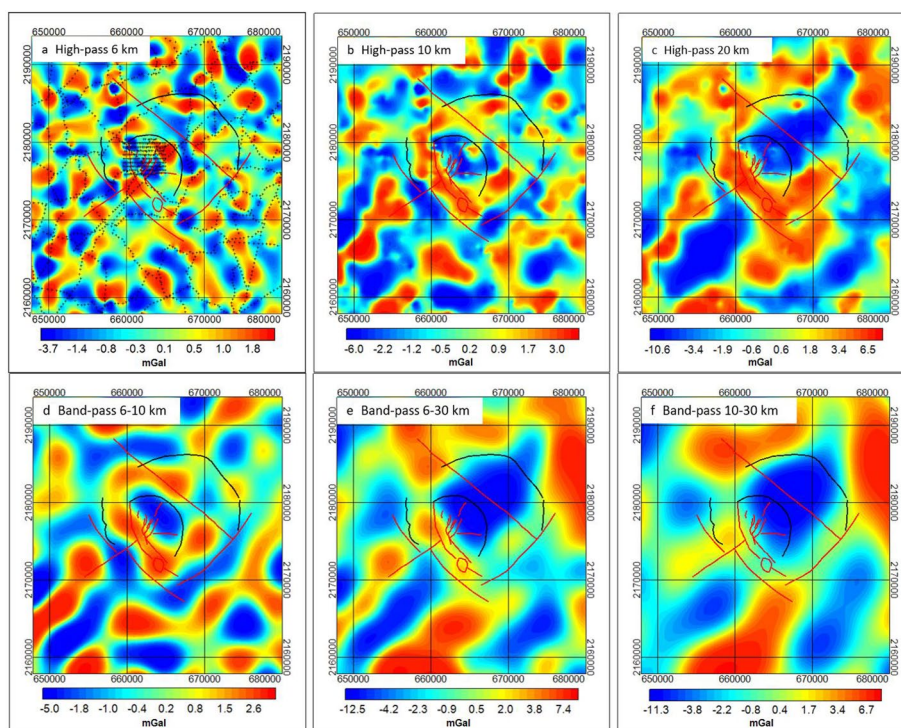


Fig. 9 Residual anomalies obtained from high-pass and band-pass filtering with corner wavelengths of 6, 10, 20, and 6–10, 6–30, and 10–30 km, respectively. Red and black lines represent major faults and the boundaries of the caldera, respectively (Calcagno et al. 2022). Black crosses represent the gravity measurement locations

longer than 20 km. The annular alignment appears to open up at this corner wavelength and turn into NE–SW and NW–SE alignments. Thus, a large low-gravity anomaly runs NE–SW across the entire caldera and beyond (Fig. 9c). However, it is intersected to the south by a NW–SE-striking high-gravity anomaly that coincides with major NW–SE-striking surface faults associated with the LHGF.

Band-pass filtering confirms the NE–SW directed positive and negative anomalies as well as the transformation of the ring-shaped structure into NW–SE-trending high anomalies and NE–SW low anomalies. Note that the NE–SW and NW–SE alignments persist through the different wavelength ranges and are assumed to represent the dominant structural setting.

Slip and dilation tendency analysis results

In the following, we first present the assumptions we have made for a generic estimate of the slip and dilation tendency analysis. It should be noted that neither the gravity nor the morpho-structure analyses provide information on the depth of the corresponding geological or tectonic structures. However, it must be assumed that they occur above or at most in the BDT. The rheological profiles of the TMVB and LHGF areas for estimating the depth of the BDT are shown in Fig. 10. Assuming a high pore fluid pressure in the LHGF, the depth of the BDT can be estimated to be between 2.5

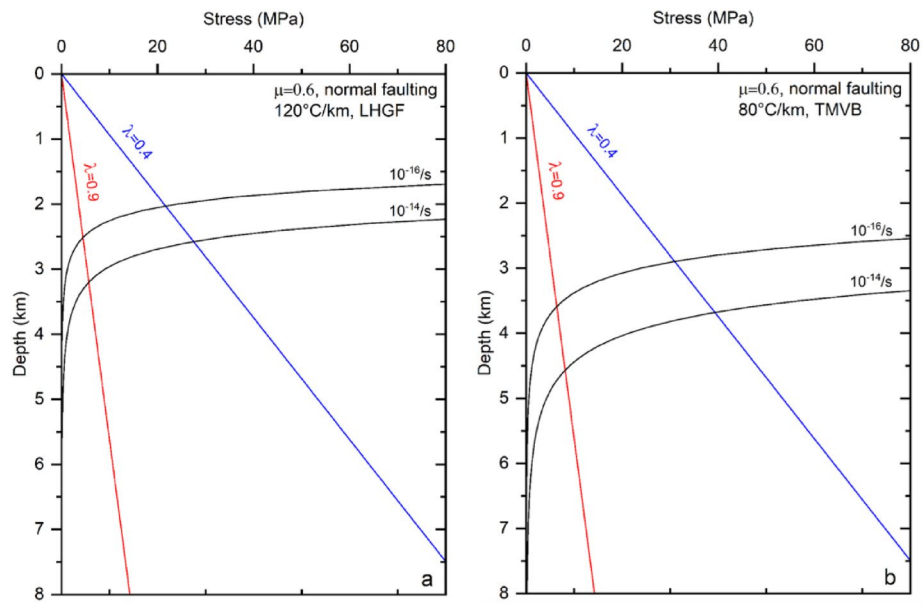


Fig. 10 Rheological profiles for the LHGF (a), and the TMVB (b). Red and blue lines delineate the geothermal fluid pressure with pore fluid factor λ inside and outside of the caldera, respectively. The latter reveals hydrostatic condition. Black lines show assumed tectonic strain rates in the ductile regime

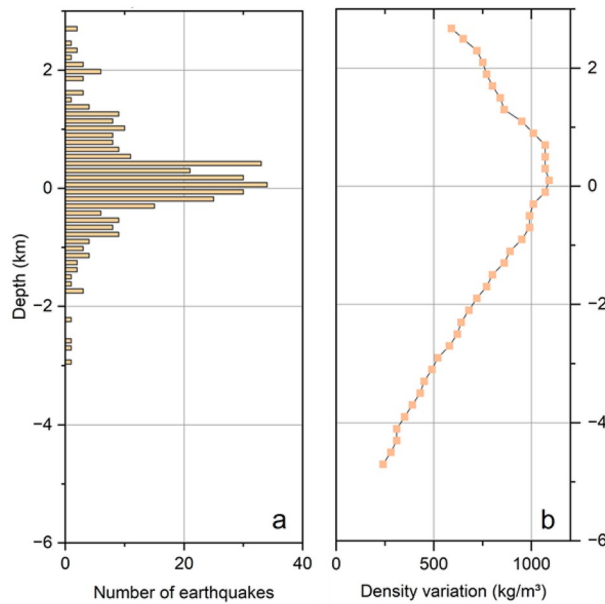


Fig. 11 a Local earthquake distribution in Los Humeros from 1-D inversion (Toledo et al. 2020), and b density variation with depth from the regional density model in Los Humeros (Carrillo et al. 2022)

and 3.3 km as a first approximation (Fig. 10a); in comparison, the depth of the BDT in the TMVB would be between 2.9 and 4.6 km for low and high pore fluid pressure, respectively (Fig. 10b).

Table 4 Total and effective principal stresses are estimated for the depth of 3.2 km, where the transition of strike-slip to normal faulting regime occurs

Total principal stress S [MPa]	Effective principal stress $\sigma = S - P_p$ [MPa]
77 (S_1)	54 (σ_1)
77 (S_2)	54 (σ_2)
39 (S_3)	16 (σ_3)

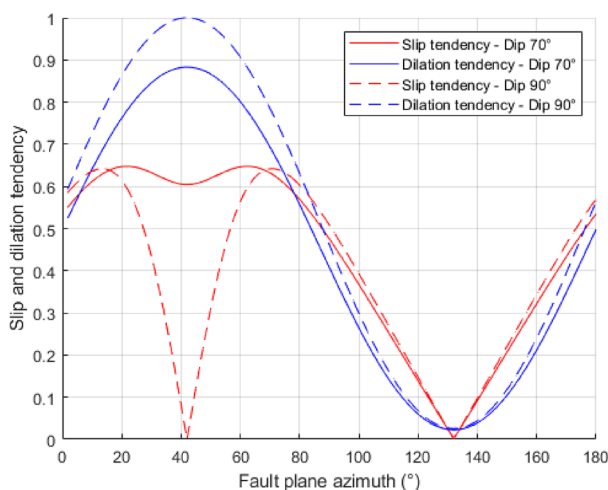


Fig. 12 Slip and dilation tendencies of 70° and 90° dipping structures as a function of the fault plane azimuth under a normal faulting regime at 3.2 km depth and a maximum horizontal stress of N42°E

To further substantiate our estimate, we refer to the results of seismic events recorded over a 12-month period in Los Humeros (Toledo et al. 2020). The peak of the event distribution is at a depth of about 3 km below ground level (Fig. 11a) and then decreases to zero at a depth of about 5–6 km. Similarly, the density values from the 3-D inversion (Carrillo et al. 2022) show a decrease from a depth of around 3 km (Fig. 11b). Lithologically, this decrease occurs within a basement that can be assumed to be homogeneous. The density decrease can thus be explained by decreasing porosity as an alternative to lithological changes. Experimental results support this assumption (Violay et al. 2017).

These observations, together with the calculations of the rheological profiles (Fig. 10), indicate that the BDT zone in the LHGF begins at a depth of about 3 km below ground level. The stress estimation results show a trans-tensional faulting regime from strike-slip to normal at 3.2 km depth and at a P_p of 23.3 MPa (Additional file 1: Fig. S8). It implies a regional trans-tensional deformation to be partitioned in the main fault trends affecting the areas. The magnitudes of the total and effective principal stresses are shown in Table 4.

Since the transition depth of 3.2 km is estimated as the upper limit of the BDT and deeper levels indicate a normal faulting regime, the generic slip and dilation tendency

analysis were performed for such a regime. Inclinations of 70° are taken into account, as the kinematic indicators show this average inclination.

The maximum of dilation tendency at θ_{SHmax} is accompanied by maxima of the slip tendency at 22° and 62° (Fig. 12). Note that increasing dip leads to a minimum of slip tendency around θ_{SHmax} . The minimum slip and dilation tendencies both occur perpendicular to θ_{SHmax} . This indicates that there is no preferential reactivation on NW–SE oriented structures, i.e., such as observed in combination with gravity highs. In contrast, structures dominated by gravity minima and NE–SW oriented may be reactivated for both opening and shearing failure if the dip tends to angles of about 70°.

Discussion

The eastern sector of the TMVB is characterized by two coeval main systems of faults, respectively, NNW- and NE-oriented (Norini et al. 2015; García-Palomo et al. 2018; Olvera-García et al. 2020a, 2020b; Gómez-Alvarez et al. 2021; Mennella et al. 2022). These two orientations were recognized in the morpho-tectonic lineaments in the study area. The kinematic meaning is suggested by the analysis of fault surfaces carried out in the Las Minas area, considered the analogue, exhumed geothermal system of Los Humeros. Here, Olvera-García et al. (2020a) recognized that the NW-oriented structures are dominantly oblique to normal, with the latter often being the last kinematic event overprinting the previous kinematic indicators, whereas the NE-oriented faults resulted in a dominantly normal movement. This different evolution has been explained considering two kinematic events: during the first, the NW-oriented crustal stretching is the prominent force, thus the NW-oriented structures play the role of transfer faults (oblique kinematics), acting with the NE-oriented normal faults; during the second event, uplift is dominant, and pre-existing structures (i.e., both NW- and NE-oriented faults) are forced to play the role of normal faults.

These oriented NE- and NW-oriented structures were also observed both in the residual anomaly map (Fig. 7b) and in the residual anomalies obtained by filtering analysis (Fig. 9). Figure 9a–c, shows how the major NE–SW as well as the NW–SE-oriented structures control the major residual anomalies, and while other minor structures (and caldera structures as well) play a subdued role in respect to those. The same relationships are highlighted in Fig. 9d, e. However, a quantitative interpretation of the anomalies is not presented in this study.

The calculated gravity carried out by forward modeling in the Los Humeros area (Fig. 8) shows a sub-circular gravity low anomaly, while the observed gravity (Fig. 7b) shows a lineal trend of a low gravity in the NE–SW direction, where the geothermal field is located. To the SW, the low gravity is interrupted by a NW–SE medium–high anomaly: an abrupt change in density between the Maxtaloya and Arenas faults (Fig. 6). This change is not only observed in density, but also in magnetization and resistivity (Corbo-Camargo et al. 2020) and limits the most productive zone of the geothermal field.

The discrepancies between the forward-modeled gravity data using an existing geological model and the observed gravity data, even after applying Butterworth filters,

underscore the complexity of the subsurface structure. The geological model may not be able to represent the complex subsurface structures and variations in gravity anomalies.

Our estimation of the stress state revealed a trans-tensional fault regime at depth in the basement, ranging from strike-slip to normal faulting. According to Kruszewski et al. (2022), a normal fault regime based on focal mechanisms predominates at depth. This suggests that deformation in the basement is more influenced by the regional stress state and less by caldera collapse, which is consistent with the resurgence hypothesized by Norini et al. (2015) and Toledo et al. (2019). These faulting regimes are in accordance with the dominant kinematic movements of the NNW- and NE-striking fault systems proposed by Olvera-García et al. (2020a). Furthermore, the latter is in agreement with the predominant NE- and NW-oriented structures obtained by our gravimetric and morpho-structural analyses.

Our analysis of slip and dilatation tendencies shows that NE–SW oriented structures have the highest reactivation potential. This orientation coincides with one of the main orientations identified in the morpho-structural (Fig. 6) and gravity analyses (Figs. 7 and 9), and with the orientation of some of the main faults present in the geological model (Fig. 3). The relationship between high reactivation potential, fracture porosity and low-gravity anomalies has already been demonstrated in various geothermal environments (Altwegg et al. 2015; Guglielmetti et al. 2013; Baillieux et al. 2014).

In contrast, other considerations can be made for the NW–SE trending faults. The latter run almost parallel to the main tectonic stretching direction and are therefore hardly exposed to dilation. This is obviously a consequence of the boundary conditions imposed by the calculation, which consider the fault orientation as the decisive factor for a favorable dilatancy. However, the parallelism between the tectonic stretching direction and the fault trend supports the interpretation that the NW–SE trending faults, which were active at the same time as the normal faults, played the role of transfer faults within the same extensional regime, as proposed by Olvera-García et al. (2020a), who studied the Los Humeros analog.

The contribution of the transfer fault zones, i.e., with strike-slip to trans-tensional kinematics, in a geothermal context, has been investigated in different areas (e.g., Alçiçek et al. 2013; Liotta and Brogi 2020; Liotta et al. 2021). The key factor is linked to the orientation of the intermediate stress axis, i.e., from vertical to oblique, determining the kinematics of each single transfer fault. As described by Sibson (2000), the intermediate stress axis mimics the orientation of the structural channels that drive fluid flow. The more vertical it is, the more efficiently the deep fluids are distributed laterally into the dilated normal faults.

Finally, it is important to mention that our analysis was based on a generic fault model since the maximum depth of each fault in the LHGF is unknown. For this reason, we estimated the BDT depth as the top of the transition zone from brittle to ductile rheological behavior, and not all faults necessarily reach that depth. They could go even deeper, as the BDT is not a sharp boundary but a transition zone, as shown by the fact that earthquakes can occur to some extent at deeper structural levels.

In this framework, the inversion of gravity field data shows that density starts to decrease at a depth of about 3 km (Fig. 11b, Carrillo et al. 2022) and that local seismic

activity peaks at this depth before decreasing (Fig. 11a, Toledo et al. 2020), as expected when the BDT is reached.

Conclusions

The morpho-structural approach and the gravimetric analysis show that the structural setting of the LHVC is mainly dominated by NE–SW and NW–SE oriented structures, which also favored the development of the Los Humeros caldera and controlled the geometry. The alignments are not only observed inside the volcanic complex, but also in the Las Minas Valley, the Perote fault in the Cofre de Perote, and to the SW of Los Humeros. These structures appear to be independent of the presence of the volcano and calderas and are therefore considered to be of tectonic origin. Furthermore, these oriented tectonic structures appear to have direct control over the emplacement of the Los Humeros volcano, as also shown by regional geology and residual anomalies.

Because the caldera collapse is a Pleistocene event and today resurgence, i.e., uplift, is considered effective, our slip and dilation tendency analysis was focused on the regional tectonic structures. The combination of high reactivation potential and low gravity along regionally significant structures that are NE–SW oriented in the study area indicates fracture porosity as the cause of the low gravity.

Supplementary Information

The online version contains supplementary material available at <https://doi.org/10.1186/s40517-024-00285-7>.

Additional file 1: Figure S1. Los Humeros volcano, with location of figures discussed in this supplementary material. Red lines: faults. Purple lines: craters and crater rims. Dashed orange lines: buried volcano-tectonic features. DEM (15 m) is from Servicio Geológico Mexicano, <https://www.sgm.gob.mx/GeolInfoMexGobMx/>. **Figure S2. a** Arenas fault. The coexistence of several morpho-structures (tectonic escarpments, alignment of craters and monogenic cones, breaching of crater rims) identify the lineament shown in figure as a normal fault, dipping to the southwest, acting as conduit for volcanic eruptions. **b** Directions of lava flows (redrawn from Carrasco-Nunez et al. 2012, with further data from this work) document the fissural eruptions of lavas from the NE-oriented Arenas fault and of the NW-oriented Hidalgo fault, from at least 7.3 ka (El Limon lava flow) and as recent as 2.8 ka B.P. (El Pajaro lava flow). **Figure S3. a** Geological map (Carrasco-Nunez et al. 2012) and DEM (15 m) is from Servicio Geológico Mexicano, <https://www.sgm.gob.mx/GeolInfoMexGobMx/> of NW sector of Los Humeros. Parallel and laterally continuous geomorphological scarps are evident, cutting through the Rhyolitic domes Middle Pleistocene paleosurface (Qr3 – here dated 220–360 ka B.P.). A component of right lateral displacement of the Rhyolitic domes is also visible. **b** Topographic profile along the Qr3 paleosurface, orthogonal to the morpho-structure interpreted as fault (vertical slip rate across the fault system is about 0.27 mm/a). **c** Detail of a relevant holocenic volcanic crater (3.9–2.8 ka B.P., emplaced on the olivine basaltic lavas, Qb1 – 3.9 ka, and filled by El Pajaro trachytes, Qt1 – 2.8 ka), clearly faulted by action of the NW–SE oriented prosecution of Maxtaloya fault system to the north; this fault results aligned with the above discussed tectonic structure (red lines). Purple lines indicate the crater rim and the bottom of the relative scarp. **Figure S4. a** Geological map and DEM (15 m) of W sector of Los Humeros, at Oyameles. Parallel and laterally continuous geomorphological scarps are evident, cutting through the Rhyolitic domes Middle Pleistocene paleosurface (Qr3 – here dated 270 ± 17 ka B.P.). **b** Topographic profile along the Qr3 paleosurface, orthogonal to the morpho-structure interpreted as fault (vertical slip rate is about 0.22 mm/a). **c** A few minor faults are visible in volcanic deposits (Qr3) in an abandoned quarry. Their dip azimuth varies between N107° and N125°, dipping 70 up to 85° toward the SE (structural data available on <https://gemex.d4science.org/group/gemex>). These can be interpreted as secondary minor structures associated to the main faults (similar to the secondary structures associated to the Maxtaloya fault, see Fig. 5a). **d** Major fault is visible in the volcanic deposit at station S1. Fault dip azimuth is N280°, dipping 60° toward the west, bedding is N245°/45° (dip azimuth, dip). Photos by Piccardi et al. 2017. **Figure S5. a** Central sector of the NW–SE oriented Maxtaloya fault displayed on a 1 m resolution DEM (kindly provided by CeMie-Geo project). The series of secondary structures, whose dip azimuth range from N90° to N130°, arranged en echelon visible in the southern part of the image along the fault is indicative of a subdued component of dextral horizontal slip on the main fault. Kinematic indicator measured on the main fault plane at Station S4 show normal oblique slip with subdued component of dextral slip (dip azimuth ranging from N230° to N260°, dip from 52° to 88°, pitch from – 75 to – 88) (structural data available on <https://gemex.d4science.org/group/gemex>). **b** Main fault plane of the Maxtaloya fault at Station S3 (in Fig. 5a). The fault plane exhibits clear kinematic indicators such as striae, grooves, mineralized veins and others, showing mostly dip slip (pitch ranging from +70 to – 80). Nevertheless, at one place two superimposed generation of striae have been recognized, with N235°, 62, – 83 over N233°, 60, +85 (dip azimuth, dip, pitch), with the dextral component of slip resulting the most recent one. Dextral component of slip on the Maxtaloya fault

observed here is coherent with the dextral displacement of the Rhyolitic domes depicted in Fig. S3a. Men give scale. **Figure S6.** Radially average power spectrum of the Complete Bouguer Anomaly (Figure 5a of the main manuscript). A cutoff wavelength of 20.5 km was selected to separate the lower and higher frequencies, related to regional and local anomalies, respectively. The cutoff wavelength was chosen where the slope of the power spectrum changes, indicating a change in the depth of the anomalous source. **Figure S7.** Location of the kinematic indicators collected on the main structures within Los Potreros caldera (Table 1) displayed on a 1 m high-resolution DEM (kindly provided by CeMie-Geo project). See the kinematic indicators associated to these structures in Table S1. **Figure S8.** Average total principal stresses and pore pressure with depth in Los Humeros area. A strike-slip to normal faulting regime transition is observed at 3.3 km depth at a P_p of 23.83 MPa. **Table S1.** Summarized kinematic indicators collected on dominant normal faulting main structures within the Los Potreros caldera. Average fault dip: 70°.

Acknowledgements

The authors wish to thank the Comisión Federal de Electricidad (CFE, Mexico, www.cfe.mx) for providing access and support during fieldwork and the Comisión Nacional de Hidrocarburos (CNH, Mexico, <https://www.gob.mx/cnh>) for providing the regional gravity data. The authors also would like to thank CICESE for the technical and logistical support in the field, especially Juan Omar Hernandez. We want to thank Jesús Ortigoza, Rafael Vargas, Maximiliano Pavez, and Sebastian Held for their important support during the fieldwork. We also want to thank the CeMieGEO project and Dr. Gerardo Carrasco-Núñez for providing us with the 1m Digital Elevation Model, and Tania Toledo and Philippe Jousset for providing us the final seismological catalog of Los Humeros.

Author contributions

NCT: processing and analysis of the local gravity data, analysis of the regional gravity data, stress state estimation, BDT depth estimation, slip and dilation tendency analysis, writing. NCT and JC: gravity data measurements. DL: field investigation, writing, review and editing. LP: morpho-structural analyses, field investigation, writing, review and editing. AB: field investigation, review and editing. PC: 3-D geological model. MK: tectonic strains, review and editing. ES: writing of parts of the manuscript. ES, IS, PC, MP and JC: review and editing. All authors read and approved the final manuscript.

Funding

Open Access funding enabled and organized by Projekt DEAL. This work was carried out in the framework of the GEMex project, which received funding from the European Union's EU Horizon 2020 research and innovation program under Grant agreement No. 727550 and the Mexican government under grant agreement No. 268074 (<http://www.gemex-h2020.eu>). Eva Schill and Natalia Cornejo-Triviño acknowledge funding through the program Materials and Technologies for the Energy Transition (MTET) of the Helmholtz Association.

Availability of data and materials

The datasets generated and analyzed during the current study within the framework of the GEMex project are available in the GEMex Open Access DB repository <https://gemex.igg.cnr.it>. The gravity data that support the findings of this study at regional scale were kindly provided by the Comisión Nacional de Hidrocarburos (<http://www.gob.mx/cnh>), but restrictions apply to the availability of these data, which were used under license for the current study, and so are not publicly available.

Declarations

Competing interests

The authors declare that they have no competing interests.

Received: 27 October 2021 Accepted: 20 February 2024

Published online: 15 March 2024

References

- Abdelfettah Y, Schill E, Kuhn P. Characterization of geothermally relevant structures at the top of crystalline basement in Switzerland by filters and gravity forward modelling. *Geophys J Int.* 2014;199(1):226–41. <https://doi.org/10.1093/gji/ggu255>.
- Agnew DC. Earth Tides. In: *Treatise on Geophysics*: Elsevier, pp. 163–195. <https://doi.org/10.1016/B978-0-444-52748-6.00056-0>
- Agnew DC. SPOTL: Some Programs for Ocean-Tide Loading Scripps Institution of Oceanography. SIO Technical Report. 2012.
- Alçiçek MC, Brogi A, Capezzuoli E, Liotta D, Meccheri M. Superimposed basin formation during neogene-quaternary extensional tectonics in SW-anatolia (Turkey): insights from the kinematics of the Dinar Fault Zone. *Tectonophysics.* 2013;608:713–27. <https://doi.org/10.1016/j.tecto.2013.08.008>.
- Altwegg P, Schill E, Abdelfettah Y, Radogna P-V, Mauri G. Toward fracture porosity assessment by gravity forward modeling for geothermal exploration (Sankt Gallen, Switzerland). *Geothermics.* 2015;57:26–38. <https://doi.org/10.1016/j.geothermics.2015.05.006>.
- Arellano VM, García A, Barragán RM, Izquierdo G, Aragón A, Nieva D. An updated conceptual model of the Los Humeros geothermal reservoir (Mexico). *J Volcanol Geotherm Res.* 2003;124(1–2):67–88.

- Baillieux P, Schill E, Edel J-B, Mauri G. Localization of temperature anomalies in the Upper Rhine Graben: insights from geophysics and neotectonic activity. *Int Geol Rev.* 2013;55(14):1744–62. <https://doi.org/10.1080/00206814.2013.794914>.
- Baillieux P, Schill E, Abdelfettah Y, Dezayes C. Possible natural fluid pathways from gravity pseudo-tomography in the geothermal fields of Northern Alsace (Upper Rhine Graben). *Geotherm Energy.* 2014. <https://doi.org/10.1186/s40517-014-0016-y>.
- Benediktsdóttir A, Hersir GP, Vilhalmsson AM, Manzella A, Santilano A, Held S. Report on resistivity modelling and comparison with other SHGS. Deliverable D5.2, WP5. GEMex H2020 project. 2019.
- Bertrand EA, Caldwell TG, Hill GJ, Wallin EL, Bennie SL, Cozens N, et al. Magnetotelluric imaging of upper-crustal convection plumes beneath the Taupo Volcanic Zone, New Zealand. *Geophys Res Lett.* 2012. <https://doi.org/10.1029/2011GL050177>.
- Blanton TL, Olson JE. Stress magnitudes from logs: effects of tectonic strains and temperature. *SPE Reserv Eval Eng.* 1999;2(01):62–8. <https://doi.org/10.2118/54653-PA>.
- Boccaletti M, Bonini M, Mazzuoli R, Abebe B, Piccardi L, Tortorici L. Quaternary oblique extensional tectonics in the Ethiopian Rift (Horn of Africa). *Tectonophysics.* 1998;287(1–4):97–116. [https://doi.org/10.1016/S0040-1951\(98\)80063-2](https://doi.org/10.1016/S0040-1951(98)80063-2).
- Boccaletti M, Corti G, Gasperini P, Piccardi L, Vannucci G, Clemente S. Active tectonics and seismic zonation and of the urban area of Florence (Italy). *Pure Appl Geophys.* 2001;158:2313–32. <https://doi.org/10.1007/PL00001172>.
- Boccaletti M, Corti G, Gasperini P, Piccardi L, Vannucci G, Clemente S. Active tectonics and seismic zonation of the urban area of Florence, Italy. In: Roca A, Oliveira C, editors. *Earthquake microzonation*. Basel: Birkhäuser; 2002. p. 2313–32.
- Mennella L, Brogi A, Liotta D, Giner Robles JL, Garduño-Monroy VH. Definición del campo de esfuerzos-deformación y sismotectónica del sistema de fallas Morelia-Acambay, México. *Rev Mexic Geol.* 2022;39(1):82–99. <https://doi.org/10.22201/cgeo.20072902e.2022.1.1688>.
- Bryan CJ, Sherburn S, Bibby HM, Bannister SC, Hurst AW. Shallow seismicity of the central Taupo Volcanic Zone, New Zealand: its distribution and nature. *N Z J Geol Geophys.* 1999;42(4):533–42. <https://doi.org/10.1080/00288306.1999.9514859>.
- Butterworth S. On the theory of filter amplifiers. *Exp Wirel Wirel Eng.* 1930;7:536–41.
- Byerlee J. Friction of rocks. *Pageoph.* 1978;116(4–5):615–26. <https://doi.org/10.1007/BF00876528>.
- Calcagno P, Chilès JP, Courrioux G, Guillen A. Geological modelling from field data and geological knowledge. *Phys Earth Planet Inter.* 2008;171(1–4):147–57. <https://doi.org/10.1016/j.pepi.2008.06.013>.
- Calcagno P, Evanno G, Trumpy E, Gutiérrez-Negrín LC, Macías JL, Carrasco-Núñez G, Liotta D. Preliminary 3-D geological models of Los Humeros and Acozulco geothermal fields (Mexico)—H2020 GEMex project. *Adv Geosci.* 2018;45:321–33. <https://doi.org/10.5194/adgeo-45-321-2018>.
- Calcagno P, Trumpy E, Gutiérrez-Negrín LC, Norini G, Macías JL, Carrasco-Núñez G, et al. Updating the 3D geomodels of Los Humeros and Acozulco geothermal systems (Mexico)—H2020 GEMex project. 2019. *Adv Geosci.* <https://doi.org/10.5194/adgeo-45-321-2018>.
- Calcagno P, Trumpy E, Gutiérrez-Negrín LC, Liotta D. A collection of 3D geomodels of the Los Humeros and Acozulco geothermal systems (Mexico). *Sci Data.* 2022;9(1):280. <https://doi.org/10.1038/s41597-022-01327-0>.
- Carrasco-Núñez G, McCurry M, Branney MJ, Norry M, Willcox C. Complex magma mixing, mingling, and withdrawal associated with an intra-Plinian ignimbrite eruption at a large silicic caldera volcano: Los Humeros of central Mexico. *Geol Soc Am Bull.* 2012;124(11–12):1793–809. <https://doi.org/10.1130/B30501.1>.
- Carrasco-Núñez G, López-Martínez M, Hernández J, Vargas V. Subsurface stratigraphy and its correlation with the surficial geology at Los Humeros geothermal field, eastern Trans-Mexican Volcanic Belt. *Geothermics.* 2017a;67:1–17. <https://doi.org/10.1016/j.geothermics.2017.01.001>.
- Carrasco-Núñez G, Hernández J, De León L, Dávila P, Norini G, Bernal JP. Geologic Map of Los Humeros volcanic complex and geothermal field, eastern Trans-Mexican Volcanic Belt. *Terra Digit.* 2017b;1(2):1–11. <https://doi.org/10.22201/igg.terradigitalis.2017.2.24.78>.
- Carrasco-Núñez G, Cavazos-Alvarez J, Dávila-Harris P, Bonini M, Giordano G, Corbo-Camargo F, et al. Assembly and development of large active calderas hosting geothermal systems: Insights from Los Humeros volcanic complex (Mexico). *J S Am Earth Sci.* 2022;120: 104056. <https://doi.org/10.1016/j.jsames.2022.104056>.
- Carrillo J, Perez-Flores MA, Gallardo LA, Schill E. Joint inversion of gravity and magnetic data using correspondence maps with application to geothermal fields. *Geophys J Int.* 2022;228(3):1621–36. <https://doi.org/10.1093/gji/ggab416>.
- Cattin R, Mazzotti S, Baratin L-M. GravProcess: an easy-to-use MATLAB software to process campaign gravity data and evaluate the associated uncertainties. *Comput Geosci.* 2015;81:20–7. <https://doi.org/10.1016/j.cageo.2015.04.005>.
- Cladouhos TT, Petty S, Bonneville A, Schultz A, Sorlie CF. Super hot EGS and the Newberry Deep Drilling Project. In: Cladouhos TT, Petty S, Bonneville A, Schultz A, Sorlie CF, editors. *43rd workshop on geothermal reservoir engineering*. Stanford: Stanford University; 2018.
- Corbi F, Rivalta E, Pinel V, Maccaferri F, Bagnardi M, Acocella V. How caldera collapse shapes the shallow emplacement and transfer of magma in active volcanoes. *Earth Planet Sci Lett.* 2015;431:287–93. <https://doi.org/10.1016/j.epsl.2015.09.028>.
- Corbo-Camargo F, Arzate J, Fregoso E, Norini G, Carrasco-Núñez G, Yutsis V, et al. Shallow structure of Los Humeros (LH) caldera and geothermal reservoir from magnetotellurics and potential field data. *Geophys J Int.* 2020;223(1):666–75. <https://doi.org/10.1093/gji/ggaa338>.
- Delle Donne D, Piccardi L, Odum JK, Stephenson WJ, Williams RA. High-resolution shallow reflection seismic image and surface evidence of the Upper Tiber Basin active faults (Northern Apennines Italy). *Ital J Geosci.* 2007;126:323–31.
- Espinoza-Ojeda OM, Prol-Ledesma RM, Muñoz-Jauregui JA. Update and review of continental conductive surface heat flow measurements in México: an analysis of deep boreholes. *Nat Resour Res.* 2023;32(3):981–1005. <https://doi.org/10.1007/s11053-023-10173-9>.
- Ferrari L, Orozco-Esquivel T, Manea V, Manea M. The dynamic history of the Trans-Mexican Volcanic Belt and the Mexico subduction zone. *Tectonophysics.* 2012;522–523:122–49. <https://doi.org/10.1016/j.tecto.2011.09.018>.
- Ferrill DA, Winterle J, Wittmeyer G, Sims D, Colton S, Armstrong A, Morris AP. Stressed rock strains groundwater at Yucca Mountain, Nevada. *GSA Today.* 1999;9(5):1–8.

- Ferriz H, Mahood GA. Eruption rates and compositional trends at Los Humeros Volcanic Center, Puebla, Mexico. *J Geophys Res.* 1984;89(B10):8511. <https://doi.org/10.1029/JB089iB10p08511>.
- García-Hernández OH, Ávila Olivera JA, Muñoz Jauregui A, Garduño Monroy VH, Najera Blas S, Cañas Ramírez JC, et al. Differential GPS monitoring to know the relationship between the current stress field, the active tectonic structures and the fluids circulation in the geothermal zones of Acoculco and Los Humeros, Puebla, Mexico. Reykjavik: World Geothermal Congress; 2021.
- García-Palomo A, Macías JL, Jiménez A, Tolson G, Mena M, Sánchez-Núñez JM, et al. NW-SE Pliocene-Quaternary extension in the Apan-Acoculco region, eastern Trans-Mexican Volcanic Belt. *J Volcanol Geotherm Res.* 2018;349:240–55. <https://doi.org/10.1016/j.jvolgeores.2017.11.005>.
- Giaquinta A, Boccaletti S, Boccaletti M, Piccardi L, Arecchi FT. Investigating the fractal properties of geological fault systems: the Main Ethiopian Rift Case. *Geophys Res Lett.* 1999;26(11):1633–6. <https://doi.org/10.1029/1999GL900319>.
- Gómez-Alvarez F, Garduño-Monroy VH, Sosa-Ceballos G, Jiménez-Haro A, Liotta D, Gaitan-Ramírez MF, et al. New constraints on tectonism and magmatism from the eastern sector of the Trans-Mexican Volcanic Belt (Chignahuapan Horst, Puebla, México). *J S Am Earth Sci.* 2021;112:103468. <https://doi.org/10.1016/j.jsames.2021.103468>.
- Gudnason EA, Agustsson K, Gunnarsson K, Flóvenz ÓG. Seismic activity on Reykjanes December 2014–November 2015. ÍSOR-2015/068. Iceland GeoSurvey. 2015.
- Gudnason EA, Agustsson K, Gunnarsson K, Flóvenz ÓG. Seismic activity on Reykjanes December 2015–November 2016. ÍSOR-2016/090. Iceland GeoSurvey. 2016.
- Guglielmetti L, Comina C, Abdelfettah Y, Schill E, Mandrone G. Integration of 3D geological modeling and gravity surveys for geothermal prospection in an Alpine region. *Tectonophysics.* 2013;608:1025–36. <https://doi.org/10.1016/j.tecto.2013.07.012>.
- Guillen A, Calcagno Ph, Courrioux G, Joly A, Ledru P. Geological modelling from field data and geological knowledge. *Phys Earth Planet Inter.* 2008;171(1–4):158–69. <https://doi.org/10.1016/j.pepi.2008.06.014>.
- Gutierrez-Negrin LCA, Izquierdo-Montalvo G. Review and Update of the Main Features of the Los Humeros Geothermal Field, Mexico. Bali: World Geothermal Congress; 2010.
- Heidbach O, Rajabi M, Reiter K, Ziegler M, WSM Team. World stress map database release 2016. GFZ Data Serv. 2016;10:1.
- Holohan EP, Walter TR, Schöpfer MP, Walsh JJ, van Wyk de Vries B, Troll VR. Origins of oblique-slip faulting during caldera subsidence. *GR Solid Earth.* 2013;118(4):1778–94. <https://doi.org/10.1002/jgrb.50057>.
- Holstein H. Gravimagnetic anomaly formulas for polyhedra of spatially linear media. *Geophysics.* 2003;68(1):157–67. <https://doi.org/10.1190/1.1543203>.
- Jouset P, Agustsson K, Barison E, Böhm G, Caló M, Chavarria IG et al. Seismic structures of the Acoculco and Los Humeros geothermal fields. *GEMex Deliv.* 2019.
- Kane MF. A comprehensive system of terrain corrections using a digital computer. *Geophysics.* 1962;27(4):455–62.
- Kohlstedt DL, Evans B, Mackwell SJ. Strength of the lithosphere: constraints imposed by laboratory experiments. *J Geophys Res.* 1995;100(B9):17587–602. <https://doi.org/10.1029/95JB01460>.
- Kruszewski M, Wittig V. Review of failure modes in supercritical geothermal drilling projects. *Geotherm Energy.* 2018. <https://doi.org/10.1186/s40517-018-0113-4>.
- Kruszewski M, Montegrossi G, Parisio F, Saenger EH. Borehole observation-based in situ stress state estimation of the Los Humeros geothermal field (Mexico). *Geomech Energy Environ.* 2022;32: 100392. <https://doi.org/10.1016/j.gete.2022.100392>.
- LaFehr TR. An exact solution for the gravity curvature (Bullard B) correction. *Geophysics.* 1991;56(8):1179–84.
- Lelli M, Kretzschmar TG, Cabassi J, Doveri M, Sanchez-Avila JI, Gherardi F, Magro G, Norelli F, et al. Fluid geochemistry of the Los Humeros geothermal field (LHGF - Puebla, Mexico): New constraints for the conceptual model. *Geothermics.* 2021;90:101983. <https://doi.org/10.1016/j.geothermics.2020.101983>.
- Lermo J, Lorenzo C, Antayhua Y, Ramos E, Jiménez N. Sísmica pasiva en el campo geotérmico de Los Humeros, Puebla-México y su relación con los pozos inyectoros. In: Lermo J, Lorenzo C, Antayhua Y, Ramos E, Jiménez N, editors. XVIII Congreso Peruano de Geología. Lima: Pontificia Universidad Católica del Perú; 2016.
- Liotta D, Brogi A. Pliocene-Quaternary fault kinematics in the Larderello geothermal area (Italy): Insights for the interpretation of the present stress field. *Geothermics.* 2020;83: 101714. <https://doi.org/10.1016/j.geothermics.2019.101714>.
- Liotta D, Ranalli G. Correlation between seismic reflectivity and rheology in extended lithosphere: southern Tuscany, inner Northern Apennines, Italy. *Tectonophysics.* 1999;315(1–4):109–22. [https://doi.org/10.1016/S0040-1951\(99\)00292-9](https://doi.org/10.1016/S0040-1951(99)00292-9).
- Liotta D, Brogi A, Árnadóttir S, Ágústsson K, Thorsteinsdóttir U. Field evidence of the interplay between rift and transform structures in the Krafla geothermal area, N-Iceland. *Geothermics.* 2021;91: 102039. <https://doi.org/10.1016/j.geothermics.2020.102039>.
- Lorenzo-Pulido CD. Borehole Geophysics and Geology of Well H-43, Los Humeros Geothermal Field, Puebla, México. United Nations University, Orkustofnun, Grensásvegur 9, IS-108 Reykjavík, Iceland. Reports of Geothermal Training Programme. 2008.
- Lucci F, Carrasco-Núñez G, Rossetti F, Theye T, White JC, Urbani S, et al. Anatomy of the magmatic plumbing system of Los Humeros Caldera (Mexico): implications for geothermal systems. *Solid Earth.* 2020;11(1):125–59. <https://doi.org/10.5194/se-11-125-2020>.
- Maestrelli D, Bonini M, Corti G, Del Ventisette C, Moratti G, Montanari D. Exploring fault propagation and the role of inherited structures during caldera collapse through laboratory experiments. *J Volcanol Geotherm Res.* 2021;414:107232. <https://doi.org/10.1016/j.jvolgeores.2021.107232>.
- Meixner J, Schill E, Grimmer JC, Gaucher E, Kohl T, Klingler P. Structural control of geothermal reservoirs in extensional tectonic settings: an example from the Upper Rhine Graben. *J Struct Geol.* 2016;82:1–15. <https://doi.org/10.1016/j.jsg.2015.11.003>.
- Morris A, Ferrill DA, Henderson DB. Slip tendency analysis and fault reactivation. *Geology.* 1996;24:275–8.

- Nagy D. The prism method for terrain corrections using digital computers. *Pure Appl Geophys.* 1966;63(1):31–9. <https://doi.org/10.1007/BF00875156>.
- Nirta G, Vittori E, Blumetti AM, Di Manna P, Benvenuti M, Montanari D, et al. Geomorphological and paleoseismological evidence of capable faulting in the Northern Apennines (Italy): insights into active tectonics and seismic hazard of the Lunigiana basin. *Geomorphology.* 2021;374:1–18. <https://doi.org/10.1016/j.geomorph.2020.107486>.
- Norini G, Gropelli G, Sulpizio R, Carrasco-Núñez G, Dávila-Harris P, Pelliccioli C, et al. Structural analysis and thermal remote sensing of the Los Humeros Volcanic Complex: implications for volcano structure and geothermal exploration. *J Volcanol Geother Res.* 2015;301:221–37. <https://doi.org/10.1016/j.jvolgeores.2015.05.014>.
- Norini G, Carrasco-Núñez G, Corbo-Camargo F, Lermo J, Rojas JH, Castro C, Bonini M, Montanari D, Corti G, et al. The structural architecture of the Los Humeros volcanic complex and geothermal field. *J Volcanol Geother Res.* 2019;381:312–29. <https://doi.org/10.1016/j.jvolgeores.2019.06.010>.
- Okabe M. Analytical expressions for gravity anomalies due to homogeneous polyhedral bodies and translations into magnetic anomalies. *Geophysics.* 1979;44(4):730–41. <https://doi.org/10.1190/1.1440973>.
- Oliva SJ, Ebinger CJ, Rivalta E, Williams CA, Wauthier C, Currie CA. State of stress and stress rotations: quantifying the role of surface topography and subsurface density contrasts in magmatic rift zones (Eastern Rift, Africa). *Earth Planet Sci Lett.* 2022;584: 117478. <https://doi.org/10.1016/j.epsl.2022.117478>.
- Olvera-García E, Bianco C, Víctor Hugo GM, Brogi A, Liotta D, Wheeler W, Gómez-Alvarez F, et al. Geology of Las Minas: an example of an exhumed geothermal system (Eastern Trans-Mexican Volcanic Belt). *J Maps.* 2020a;16(2):918–26. <https://doi.org/10.1080/17445647.2020.1842815>.
- Olvera-García E, Garduño-Monroy VH, Liotta D, Brogi A, Bermejo-Santoyo G, Guevara-Alday JA. Neogene-Quaternary normal and transfer faults controlling deep-seated geothermal systems: the case of San Agustín del Maíz (central Trans-Mexican Volcanic Belt, México). *Geothermics.* 2020b;86:101791. <https://doi.org/10.1016/j.geothermics.2019.101791>.
- Pavez M, Schill E, Held S, Díaz D, Kohl T. Visualizing preferential magmatic and geothermal fluid pathways via electric conductivity at Villarrica Volcano, S-Chile. *J Volcanol Geother Res.* 2020;400: 106913. <https://doi.org/10.1016/j.jvolgeores.2020.106913>.
- Piccardi L, Sani F, Bonini M, Boccaletti M, Moratti G, Gualtierotti A. Quaternary deformations in north-central Apennines evidence and implications (Deformazioni quaternarie nell'Appennino centro-settentrionale: Evidenze ed implicazioni). *Italian J Quat Sci.* 1997;10(2):273–80.
- Piccardi L, Gaudemer Y, Tapponnier P, Boccaletti M. Active oblique extension in the central Apennines (Italy): evidence from the Fucino region. *Geophys J Int.* 1999;139(2):499–530. <https://doi.org/10.1046/j.1365-246x.1999.00955.x>.
- Piccardi L, Vittori E, Blumetti AM, Comerci V, Di Manna P, Guerrieri L, et al. Mapping capable faulting hazard in a moderate-seismicity, high heat-flow environment: The Tuscia province (southern Tuscany-northern Latium, Italy). *Quat Int.* 2017;451:11–36. <https://doi.org/10.1016/j.quaint.2017.07.018>.
- Pierotti L, Gherardi F, Facca G, Piccardi L, Moratti G. Detecting CO₂ anomalies in a spring on Mt. Amiata volcano (Italy). *Phys Chem Earth Parts.* 2017;98:161–72. <https://doi.org/10.1016/j.pce.2017.01.008>.
- Plouff D. Gravity and magnetic fields of polygonal prisms and application to magnetic terrain corrections. *Geophysics.* 1976;41(4):727–41. <https://doi.org/10.1190/1.1440645>.
- Prol-Ledesma RM, Morán-Zenteno DJ. Heat flow and geothermal provinces in Mexico. *Geothermics.* 2019;78:183–200. <https://doi.org/10.1016/j.geothermics.2018.12.009>.
- Prol-Ledesma RM, Carrillo-de la Cruz JL, Torres-Verab MA, Membrillo-Abad AS, Espinoza-Ojedac OM. Heat flow map and geothermal resources in Mexico. *Terra Digit.* 2018. <https://doi.org/10.22201/igg.25940694.2018.2.51>.
- Ranalli G. *Rheology of the earth.* 2nd ed. London: Chapman & Hall; 1995.
- Ranalli G. Rheology of the lithosphere in space and time. *Geol Soc.* 1997;121(1):19–37. <https://doi.org/10.1144/GSL.SP.1997.121.01.02>.
- Regenauer-Lieb K, Petit J-P. Cutting of the European continental lithosphere: plasticity theory applied to the present Alpine collision. *J Geophys Res.* 1997;102(B4):7731–46. <https://doi.org/10.1029/96JB03409>.
- Rodríguez H, Lermo J, Urban E. Analysis of seismic anisotropy in Los Humeros geothermal field, Mexico. In: Rodríguez H, Lermo J, Urban E, editors. *Thirty-seventh workshop on geothermal reservoir engineering.* Stanford: Stanford University; 2012.
- Sæmundsson K, Einarsson P. Notes on the tectonics of Reykjanes. *ISOR-2014/003.* Iceland GeoSurvey. 2014.
- Reinsch T, Dobson P, Asanuma H, Huenges E, Poletto F, Sanjuan B. Utilizing supercritical geothermal systems: a review of past ventures and ongoing research activities. *Geotherm Energy.* 2017. <https://doi.org/10.1186/s40517-017-0075-y>.
- Sibson RH. Frictional constraints on thrust, wrench and normal faults. *Nature.* 1974;249(5457):542–4. <https://doi.org/10.1038/249542a0>.
- Sibson RH. Fluid involvement in normal faulting. *J Geodyn.* 2000;29(3–5):469–99. [https://doi.org/10.1016/s0264-3707\(99\)00042-3](https://doi.org/10.1016/s0264-3707(99)00042-3).
- Siler DL, Faulds JE, Mayhew B, McNamara DD. Analysis of the favorability for geothermal fluid flow in 3D: Astor Pass geothermal prospect, Great Basin, Northwestern Nevada, USA. *Geothermics.* 2016;60:1–12. <https://doi.org/10.1016/j.geothermics.2015.11.002>.
- Suter M. State of stress and active deformation in Mexico and western Central America. Boulder: Geological Society of America; 1991. p. 401–21. <https://doi.org/10.1130/DNAG-CSMS-NEO.401>.
- Thiercelin MJ, Plumb RA. Core-based prediction of lithologic stress contrasts in East Texas formations. *SPE Form Eval.* 1994;9(04):251–8. <https://doi.org/10.2118/21847-PA>.
- Toledo T, Gaucher E, Metz M, Calò M, Figueroa A, Angulo J, Jousset P, Kieling K, Saenger E. Dataset of the 6G seismic network at Los Humeros. Karlsruhe: Karlsruhe Institute Of Technology KIT, Geophysical Institute GPI; 2019.
- Toledo T, Gaucher E, Jousset P, Jentsch A, Haberland C, Maurer H, et al. Local earthquake tomography at Los Humeros Geothermal Field (Mexico). *JGR Solid Earth.* 2020. <https://doi.org/10.1029/2020JB020390>.
- Urrutia-Fucugauchi J, Flores-Ruiz JH. Bouguer gravity anomalies and regional crustal structure in Central Mexico. *Int Geol Rev.* 1996;38(2):176–94. <https://doi.org/10.1080/00206819709465330>.

- Violay M, Heap MJ, Acosta M, Madonna C. Porosity evolution at the brittle-ductile transition in the continental crust: Implications for deep hydro-geothermal circulation. *Sci Rep.* 2017;7(1):7705. <https://doi.org/10.1038/s41598-017-08108-5>.
- Watanabe N, Sakaguchi K, Goto R, Miura T, Yamane K, Ishibashi T, et al. Cloud-fracture networks as a means of accessing superhot geothermal energy. *Sci Rep.* 2019;9(1):939. <https://doi.org/10.1038/s41598-018-37634-z>.
- Weydt LM, Ramírez-Guzmán AA, Pola A, Lepillier B, Kummerow J, Mandrone G, et al. Petrophysical and mechanical rock property database of the Los Humeros and Acoculco geothermal fields (Mexico). *Earth Syst Sci Data.* 2021;13(2):571–98. <https://doi.org/10.5194/essd-13-571-2021>.

Publisher's Note

Springer Nature remains neutral with regard to jurisdictional claims in published maps and institutional affiliations.